PNAS RESEARCH ARTICLE | EARTH, ATMOSPHERIC, AND PLANETARY SCIENCES

Iron silicate perovskite and postperovskite in the deep lower mantle

Ziqiang Yang[a], Zijun Song[b], Zhongqing Wu[b,c,d,1], Ho-kwang Mao[a,e,1], and Li Zhang[a,1]

Contributed by Ho-kwang Mao; received January 19, 2024; accepted March 18, 2024; reviewed by Bin Chen and Zhigang Zhang

Ferromagnesian silicates are the dominant constituents of the Earth's mantle, which comprise more than 80% of our planet by volume. To interpret the low shear-velocity anomalies in the lower mantle, we need to construct a reliable transformation diagram of ferromagnesian silicates over a wide pressure–temperature (*P-T*) range. While $MgSiO_3$ in the perovskite structure has been extensively studied due to its dominance on Earth, phase transformations of iron silicates under the lower mantle conditions remain unresolved. In this study, we have obtained an iron silicate phase in the perovskite (Pv) structure using synthetic fayalite (Fe_2SiO_4) as the starting material under *P-T* conditions of the lower mantle. Chemical analyses revealed an unexpectedly high Fe/Si ratio of 1.72(3) for the Pv phase in coexistence with metallic iron particles, indicating incorporation of about 25 mol% Fe_2O_3 in the Pv phase with an approximate chemical formula $(Fe^{2+}_{0.75}Fe^{3+}_{0.25})(Fe^{3+}_{0.25}Si_{0.75})O_3$. We further obtained an iron silicate phase in the postperovskite (PPv) structure above 95 GPa. The calculated curves of compressional (V_P) and shear velocity (V_S) of iron silicate Pv and PPv as a function of pressure are nearly parallel to those of $MgSiO_3$, respectively. To the best of our knowledge, the iron silicate Pv and PPv are the densest phases among all the reported silicates stable at *P-T* conditions of the lower mantle. The high ferric iron content in the silicate phase and the spin-crossover of ferric iron at the Si-site above ~55 GPa should be taken into account in order to interpret the seismic observations. Our results would provide crucial information for constraining the geophysical and geochemical models of the lower mantle.

the lower mantle | phase transformation | perovskite | postperovskite | iron silicate

Significance

Ferromagnesian silicates are the dominant constituents of the Earth's mantle, which comprise >80% of our planet by volume. The stability and properties of iron silicates under high-pressure and high-temperature conditions would provide crucial information for explaining the mantle structure. The discovery of fayalite Fe_2SiO_4 olivine–spinel transition in 1958 marked the first known phase transition beyond the upper mantle, inspiring search for phase transformations at higher pressures. The disproportionation of fayalite spinel into mixed oxides marked the first phase transition under the lower mantle conditions. We found the disproportionation of fayalite into iron silicate perovskite above 60 GPa, or postperovskite above 95 GPa, plus metallic iron. Phase transformations of iron silicates are finally resolved over the entire mantle conditions.

There is a general consensus that the lower mantle is dominated by ferromagnesian silicates in the perovskite structure (1) known as bridgmanite (bdg). Geophysical observations indicated the existence of large-scale seismic anomalies in the Earth's deep lower mantle (DLM) (2, 3). To interpret the low shear-velocity anomalies in the DLM (4), we need to construct a reliable transformation diagram of ferromagnesian silicates over a wide pressure–temperature (*P-T*) range. While $MgSiO_3$ in the perovskite structure has been extensively studied due to its dominance on Earth, phase transformations of iron silicates remain unresolved. High pressure–temperature (*P-T*) experiments have revealed that increasing pressure can enhance the solubility of $FeSiO_3$ in the (Mg, Fe)SiO_3 perovskite (Pv) phase (5–7). So far, iron enrichment has been observed in $(Mg_{1-x}Fe_x)SiO_3$- Pv with x up to 0.74 (7) and postperovskite (PPv) with x up to 0.8 (8), respectively. The discovery of fayalite Fe_2SiO_4 olivine–spinel transition in 1958 marked the first known phase transition beyond the upper mantle (9), inspiring search for phase transformations in iron silicates at higher pressures.

Under the lower mantle conditions, it has been long believed that both Fe_2SiO_4 and $FeSiO_3$ compositions are thermodynamically unstable and will decompose into mixed oxides under high *P-T* conditions of the lower mantle (6, 10–12). Although theoretical calculations have suggested several possible high-pressure structures for the $FeSiO_3$ composition (13–15), none has yet been experimentally confirmed. On the other hand, the synthesis of a mixed-valence iron silicate Pv phase at pressures between 45 and 110 GPa using synthetic skiagite-majorite garnet as the starting material indicates that incorporation of Fe^{3+} could stabilize an iron silicate phase in the Pv structure (16). The mixed-valence state (Fe^{2+} and Fe^{3+}) and pressure-driven electronic spin transition of iron add further complexities to the crystal chemistry of iron-rich Pv phase. More importantly, the core–mantle segregation would have set the early silicate mantle dominant in ferrous iron (17). To date, it remains unclear whether iron silicates with all iron in Fe^{2+} can be stabilized in the Pv and/or PPv structures up to the extreme high *P-T* conditions of the Earth's core–mantle boundary (CMB).

In this study, we have finally synthesized iron silicates in both Pv and PPv structures using synthetic fayalite (Fe_2SiO_4) as the starting material above 60 GPa and 2,100 K, allowing us to explore the phase stability, crystal chemistry, and elasticity of the iron silicate

Author contributions: Z.Y., Z.W., H.-k.M., and L.Z. designed research; Z.Y., Z.S., Z.W., and L.Z. performed research; Z.Y., Z.S., and Z.W. analyzed data; and Z.Y., Z.S., Z.W., H.-k.M., and L.Z. wrote the paper.

Reviewers: B.C., University of Hawaii at Manoa; and Z.Z., Institute of Geology and Geophysics, Chinese Academy of Sciences.

The authors declare no competing interest.

Copyright © 2024 the Author(s). Published by PNAS. This article is distributed under Creative Commons Attribution-NonCommercial-NoDerivatives License 4.0 (CC BY-NC-ND).

[1]To whom correspondence may be addressed. Email: wuzq10@ustc.edu.cn, maohk@hpstar.ac.cn, or zhangli@hpstar.ac.cn.

This article contains supporting information online at https://www.pnas.org/lookup/suppl/doi:10.1073/pnas.2401281121/-/DCSupplemental.

Published April 15, 2024.

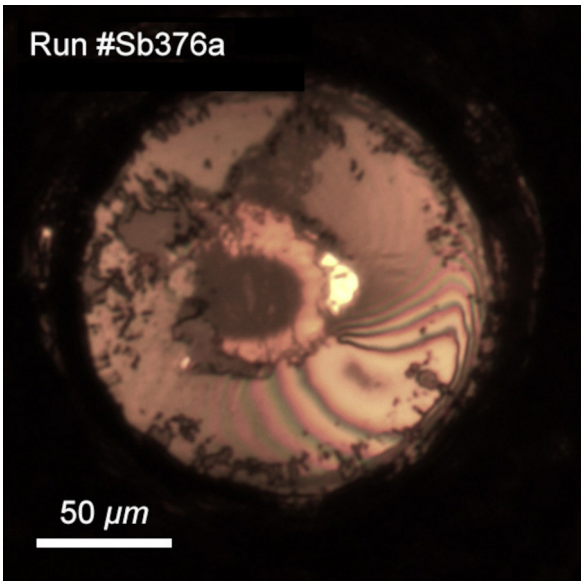

Fig. 1. A microscopic image of the sample recovered to ambient conditions from 99 GPa and 2,250 K. The laser-heated spot shows a dark color in contrast to the surrounding unheated sample.

Pv and PPv phases under high *P-T* conditions of the lower mantle. The experiments were conducted in a laser-heated diamond anvil cell (LH-DAC). The laser-heated spot can be clearly recognized under a microscope showing a color contrast with the surrounding unheated fayalite in the recovered samples (Fig. 1). The run products were characterized combining in situ synchrotron X-ray diffraction (XRD) at high-*P* after *T* quench with ex situ transmission electron microscopy coupled with energy-dispersive X-ray spectroscopy (TEM-EDS). Further, first-principles calculations were performed to obtain their elastic properties as a function of pressure.

Results and Discussion

Synthesis and Characterization of Iron Silicate Pv and PPv. A total of nine separate sets of experiments were conducted, covering *P-T* range of 52 to 119 GPa and 2,150 to 2,600 K. Experimental results and conditions are summarized in Table 1. In each run, a prepressed thin disk of synthetic fayalite Fe_2SiO_4 sandwiched between Ne or SiO_2 medium was loaded into a LH-DAC and then cold compressed to the target pressure. The double-sided laser heating system was employed to generate high temperatures and each sample was heated for 20 min at the target temperature. The run products were characterized by in situ synchrotron XRD at high-*P* after *T* quench. Our XRD measurements revealed the formation of $GdFeO_3$-type (space group: *Pbnm*) Pv phase at 63 to 99 GPa and 2,150 to 2,250 K after accounting for the thermal pressures. The observed diffraction peaks at 87 GPa after *T* quench from 2,250 K can be assigned to Pv, Ne, and Re gasket (Fig. 2 *A* and *C*, Run #Sb376a). In addition, we observed a relatively weak peak at *d*-spacing of 2.53 Å, a characteristic peak of the PPv phase, along with a set of other peaks belonging to PPv, indicating the appearance of PPv under *P-T* conditions as low as 99 GPa and 2,250 K.

To explore the stability of the PPv phase, we conducted additional experiments over a *P-T* range of 126 to 132 GPa and 2,300 to 2,500 K. To overcome the kinetic barrier in the Pv-PPv phase transformation, we compressed each fayalite sample to the target pressure prior to any heating following the suggestion from the previous study (21). Indeed, we obtained a pure $CaIrO_3$-type (space group: *Cmcm*) PPv phase at 128 GPa and 2,300 K (Fig. 2*B*, Run #Sb375a). The sharp Debye diffraction rings (Fig. 2*D* and *SI Appendix*, Fig. S1) reflect good crystallinity of the PPv phase. Contrary to the conventional view that Fe_2SiO_4 decomposes into a mixture of iron oxide and silica phases, our observations showed that iron silicates Pv and PPv can be synthesized from Fe_2SiO_4 under *P-T* conditions of the lower mantle. The Pv and PPv phases are known to have chemical formula ABX_3, where A and B are cations and X an anion. In our experiments, however, no diffraction

Table 1. Summary of the experimental conditions and results

Run#	$P_{300\,K}$ (GPa)	*T* (K)	P_T (GPa)	Medium	Phase	Unit-cell parameters				*P* scale
						a (Å)	*b* (Å)	*c* (Å)	*V* (Å^3)	
Sb510	52	2,150	63	Ne	Pv	4.6167(9)	4.8084(6)	6.646(1)	147.55(3)	V_{Ne} = 31.01(1) Å^3
Sb376b	86	2,200	97	Ne	Pv	4.492(1)	4.7399(9)	6.489(1)	138.19(3)	V_{Ne} = 27.250(8) Å^3
					PPv	Only PPv022 visible				
	18				Pv	4.796(1)	4.9779(8)	6.915(1)	165.11(3)	V_{Ne} = 39.716(8) Å^3
	10				Pv	4.864(1)	4.996(1)	6.999(1)	170.14(4)	V_{Ne} = 45.15(1) Å^3
Sb376a	87	2,250	99	Ne	Pv	4.4972(7)	4.7469(8)	6.492(1)	138.60(2)	V_{Ne} = 27.149(9) Å^3
					PPv	2.5375(6)	8.456(2)	6.316(3)	135.53(7)	
Sb506	98	2,400	111	Ne	Pv	4.443(1)	4.7286(9)	6.426(2)	135.02(3)	V_{Ne} = 26.315(8) Å^3
					PPv	2.5192(8)	8.438(3)	6.278(2)	133.46(4)	
Sa190	91	2,500	105	SiO_2	Pv	4.468(1)	4.7366(8)	6.463(1)	136.79(4)	ν_{Dia} = 1,520.0 cm^{-1}
					PPv	2.5314(9)	8.474(4)	6.280(1)	134.73(4)	
	105	2,600	119		PPv	2.5106(7)	8.394(3)	6.240(1)	131.51(4)	ν_{Dia} = 1,544.6 cm^{-1}
Sa181	112	2,500	126	Ne	PPv	2.5024(5)	8.368(1)	6.237(1)	130.60(2)	V_{Ne} = 25.378(8) Å^3
Sb375a	116	2,300	128	Ne	PPv	2.4999(5)	8.337(2)	6.220(1)	129.66(3)	V_{Ne} = 25.150(8) Å^3
Sb376c	119	2,400	132	Ne	PPv	2.4971(2)	8.320(1)	6.219(1)	129.21(2)	V_{Ne} = 25.000(8) Å^3
Sb375b	118	2,400	131	SiO_2	PPv	2.4952(3)	8.326(1)	6.2121(9)	129.06(2)	ν_{Dia} = 1,567.0 cm^{-1}

Pressures after *T* quench were determined using either the EoS of Ne (18) or the diamond Raman gauge (19). The thermal pressures were estimated based on an empirical equation *P*th = (*T*−300) × 0.0062 (GPa) which was obtained under similar *P-T* range in the previous study (20).

Downloaded from https://www.pnas.org by ZHEJIANG UNIVERSITY on April 18, 2024 from IP address 210.32.3.81.

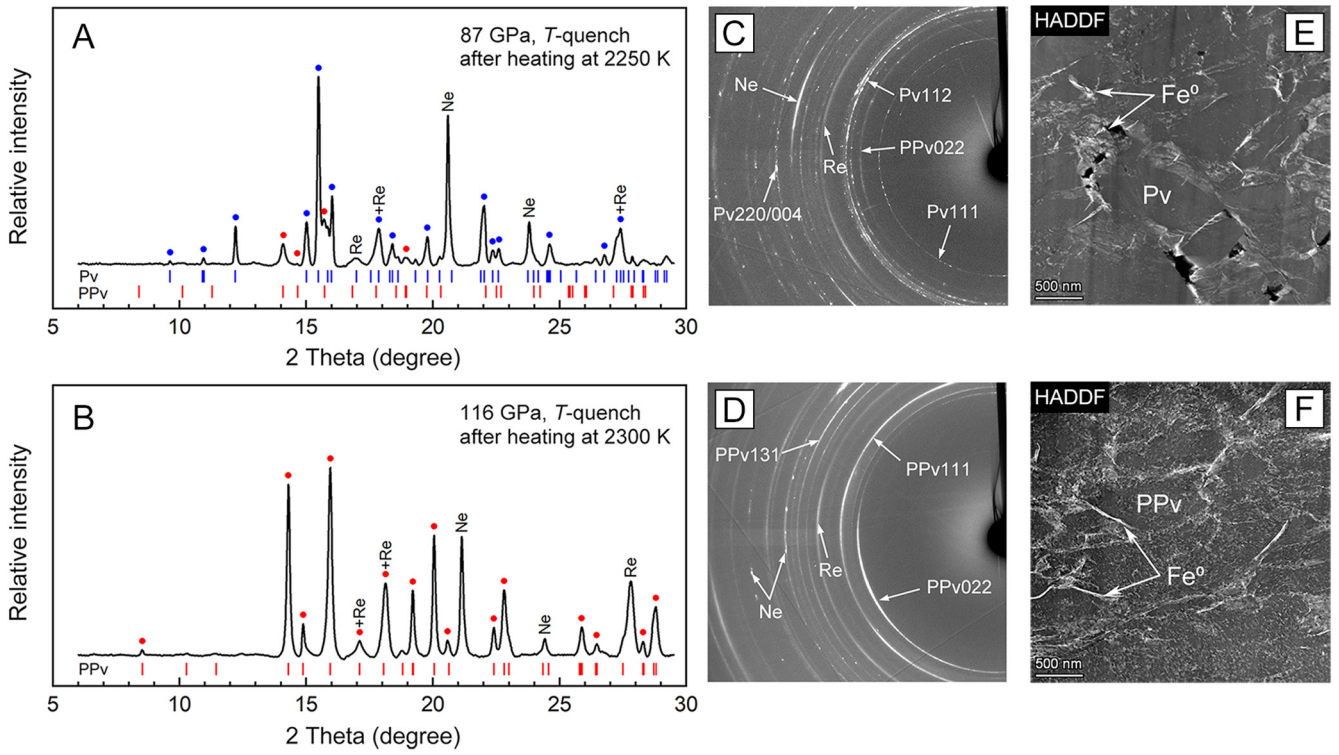

Fig. 2. In situ XRD and ex situ TEM characterization of iron silicate perovskite and postperovskite. Integrated powder XRD patterns of (*A*) iron silicate perovskite (Pv) [Run #Sb376a; space group: *Pbnm*; a = 4.4972(7) Å, b = 4.7469(8) Å, c = 6.492(1) Å, and V = 138.60(2) Å^3] and (*B*) iron silicate postperovskite (PPv) [Run #Sb375a; space group: *Cmcm*; a = 2.4999(5) Å, b = 8.337(2) Å, c = 6.220(1) Å, and V = 129.66(3) Å^3]. The corresponding two-dimensional diffraction images of Pv (*C*) and PPv (*D*) show textures of the diffraction patterns. High-angle annular dark field (HAADF) images of Pv (*E*) and PPv (*F*) show the coexistence of the silicate phase and metallic particles. The Pv and PPv phases were recovered from Run #Sb376a (87 GPa and 2,250 K) and Run #Sb375b (118 GPa and 2,400 K), respectively. The X-ray wavelength was 0.6199 Å.

Downloaded from https://www.pnas.org by ZHEJIANG UNIVERSITY on April 18, 2024 from IP address 210.32.3.81.

from FeO or any other iron oxide was observed when Fe_2SiO_4 fayalite (all iron in Fe^{2+}) was used as the starting material.

To reveal chemical composition of the iron silicate Pv and PPv phases, we further performed ex situ chemical analyses on the recovered samples. We observed that the Pv phase remained crystalline down to 10 GPa during decompression but turned amorphous after the pressure release to ambient conditions. A thin cross-section was lifted out from the heated center and prepared for the TEM analysis using a focused ion beam (FIB). The TEM images (E and F) in Fig. 2 show submicron-sized grains of the Pv and PPv phases in coexistence with metallic particles, respectively. The metallic particles of tens of nanometers in size are evenly distributed among the silicate grains (Fig. 2 *E* and *F* and *SI Appendix*, Fig. S2), but its diffraction was absent in the XRD pattern possibly due to its low crystallinity. We obtained the Fe/Si ratio of 1.72(3) in the Pv phase (*SI Appendix*, Table S1). The widespread metallic particles prevented us from obtaining the chemical composition of the PPv phase (Fig. 2*F* and *SI Appendix*, Fig. S2) but its Fe/Si ratio could be higher than that of Pv based on the distribution and proportion of the metallic particles. For simplicity, we assume the PPv phase having the same composition as the Pv phase in the following discussion. The phase assemblages and chemical analysis indicate the occurrence of disproportionation of Fe^{2+} into Fe^{3+} and Fe metal, $3Fe^{2+} = 2Fe^{3+} + Fe^0$.

We report both iron silicate Pv and PPv phases obtaining from a starting material with all iron in Fe^{2+} and the iron silicates Pv with a Fe/Si ratio of 1.72(3) is the most iron-enriched silicate among all the reported silicate phases under *P-T* conditions of the lower mantle. The physical and chemical properties of the iron silicates Pv and PPv would provide important constraints on the lower mantle models. First, iron enrichment can greatly increase the density of both Pv and PPv phases (22). In Fig. 3*A*, we plotted the density (ρ) of the iron silicate Pv and PPv phases, together with ferromagnesian silicate Pv (7, 16, 23–25) and PPv (26–28) from the previous studies, as a function of iron concentration [X_{Fe} = Fe/(Mg+Fe+Si)], respectively. The least-squares fits yield linear relationships $\rho_{Pv} = 5.12(1) + 2.47(3)X_{Fe}$ for Pv at 87 GPa and $\rho_{PPv} = 5.48(1) + 2.66(3)X_{Fe}$ for PPv at 118 GPa, respectively. We noticed that the iron silicate $(Fe^{2+}_{0.64}Fe^{3+}_{0.24})SiO_3$-Pv from the previous study has a density of ~2.2% lower than the linear fit, which might be attributed to the presence of a significant amount of vacancies (~12%) at the A-site (16). Second, according to the charge-coupled substitution, $2Fe^{3+} \rightarrow Fe^{2+} + Si^{4+}$, we obtained an approximate chemical formula $(Fe^{2+}_{0.75}Fe^{3+}_{0.25})(Fe^{3+}_{0.25}Si_{0.75})O_3$ with $X_{Fe} = 0.625$ from the Fe/Si ratio measured for the Pv phase. The disproportionation reaction of Fe_2SiO_4 into Pv plus metallic iron can be described as

$$3Fe_2SiO_4 = 4(Fe^{2+}_{0.75}Fe^{3+}_{0.25})(Fe^{3+}_{0.25}Si_{0.75})O_3 + Fe^0. \quad [1]$$

Pv-to-PPv Phase Transition in Iron Silicate. In this study, we have identified a wide two-phase coexistence field for Pv and PPv in $(Fe^{2+}, Fe^{3+})(Fe^{3+}, Si)O_3$ (Fig. 3*B*), which can be regarded as Fe_2O_3-$FeSiO_3$ solid solutions. Below 100 GPa at 2,200 to 2,250 K, PPv exists only as a minor phase (Fig. 2*A* and *SI Appendix*, Fig. S3*A*), whereas the PPv and Pv phases have comparable intensities (*SI Appendix*, Fig. S4) in experiments at 105 to 111 GPa and 2,400 to 2,500 K. A pure PPv phase was obtained above 120 GPa and 2,300 to 2,600 K. Assuming the same Clapeyron slope as the Pv-PPv transition in $MgSiO_3$ (29), we can place a rough constraint on the Pv-PPv phase boundary with the PPv-in line at 95 GPa and the Pv-out line at 113 GPa along a normal mantle geotherm (30).

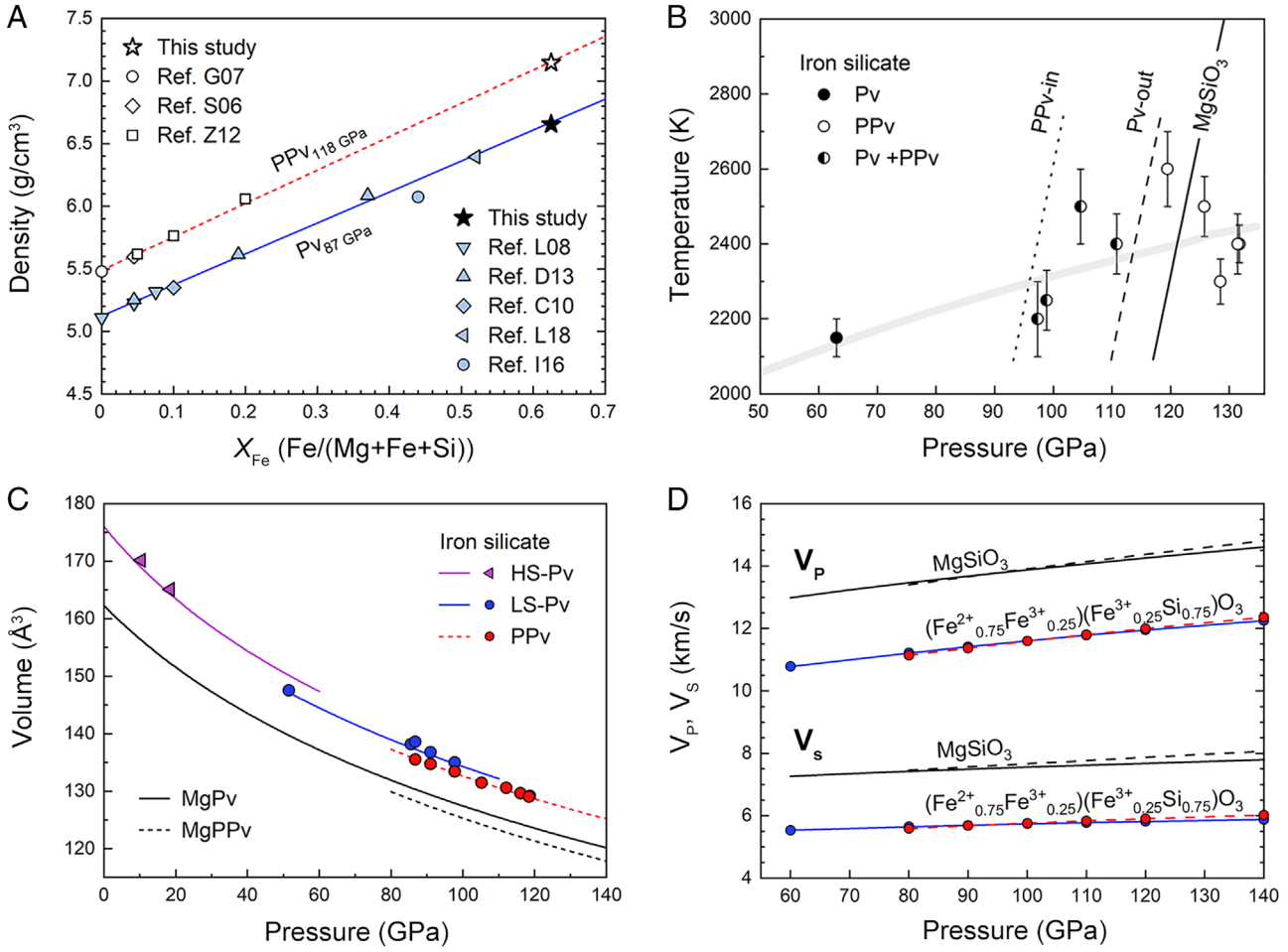

Fig. 3. Density, stability, equation of state, and elastic wave velocities of the iron silicate Pv and PPv. (*A*) Density of Pv and PPv versus iron content X_{Fe}, where X_{Fe} = Fe/(Mg+Fe+Si) in atomic ratio. Experimental data of Pv from D13 and L08 (7, 24) and PPv from G07, S06, and Z12 (26–28) were synthesized from starting materials with all iron in Fe^{2+}, whereas Pv from I16, C10, and L18 (16, 23, 25) were synthesized from Fe^{3+}-bearing starting materials. The blue solid and red dashed lines are the linear fits for Pv at 87 GPa and PPv at 118 GPa, respectively. (*B*) The stability field of iron silicate Pv and PPv. The black solid line shows the Pv-to-PPv transition boundary for $MgSiO_3$ (29). We assume the same Clapeyron slope (+13.3 MPa/K) for the iron silicate Pv-to-PPv transition. The thick gray solid line represents a normal lower-mantle geotherm (30). (*C*) Unit-cell volumes of iron silicate Pv and PPv as a function of pressure. The unit-cell volumes obtained from experiments are shown with solid symbols, whereas the computed EoS are shown with solid lines for Pv and dashed line for PPv, respectively. The EoS for $MgSiO_3$ Pv (24) and PPv (26) are plotted for comparison. (*D*) Computed static compressional (V_p) and shear (V_s) velocities of iron silicate Pv (solid lines) and PPv (dashed lines) as a function of pressure. The elastic wave velocities of $MgSiO_3$ Pv (31) and PPv (32) are shown in black solid and dashed lines, respectively.

In the solid solution series Fe_2O_3-$FeSiO_3$, the Pv to PPv transition in Fe_2O_3 occurs at 60 to 70 GPa (33, 34), lower than 95 GPa at which the PPv phase appears in $(Fe^{2+}, Fe^{3+})(Fe^{3+}, Si)O_3$, implying that an increase of Fe_2O_3 content in $FeSiO_3$ will decrease the pressure for the Pv-to-PPv transition relative to the endmember $FeSiO_3$, although neither Pv nor PPv has been experimentally synthesized in $FeSiO_3$ up to now.

Compressibility and Elastic Properties of Pv and PPv. We further investigated physical properties of the Pv and PPv phases with a chemical formula $(Fe^{2+}_{0.75}Fe^{3+}_{0.25})(Fe^{3+}_{0.25}Si_{0.75})O_3$ using first-principles calculations. Our calculated static enthalpy difference revealed a high-spin (HS) to low-spin (LS) transition of the octahedrally coordinated Fe^{3+} in the Pv structure at ~55 GPa (*SI Appendix*, Fig. S5) accompanied by a volume reduction of ~2.0% ($\Delta V_{HS\text{-}LS}$). The spin-crossover-induced volume collapse in Fe^{3+}-bearing Pv is linearly dependent on the Fe^{3+} content at the B-site (35), which has been previously confirmed by both experiments and theoretical calculations (25, 36). The predicted $\Delta V_{HS\text{-}LS}$ in $(Fe^{2+}_{0.75}Fe^{3+}_{0.25})(Fe^{3+}_{0.25}Si_{0.75})O_3$-Pv with 25% Fe^{3+} at the B-site in our study is consistent with the linear relationship, in comparison to ~4.3% volume reduction with 50% Fe^{3+} at the Si-site (36). The *P-V* relationship obtained in our decompression experiments further confirmed the volume reduction as a result of the HS-LS transition of Si-site Fe^{3+} (Fig. 3*C* and *SI Appendix*, Fig. S3).

We obtained the third Birch-Murnaghan equation of state (EoS) and the parameters are listed in *SI Appendix*, Table S2. The computed EoS showed excellent agreement with our experimental data (Fig. 3*C*), which in turn supports the occurrence of the $2Fe^{3+} \rightarrow Fe^{2+} + Si^{4+}$ charge-coupled substitution. Our results indicate that the bulk moduli of both LS-Pv and LS-PPv in $(Fe^{2+}_{0.75}Fe^{3+}_{0.25})(Fe^{3+}_{0.25}Si_{0.75})O_3$ are similar to those of $MgSiO_3$-Pv (24) and PPv (26), referred to as MgPv and MgPPv hereafter, indicating a negligible effect of iron content on the compressibility of both Pv and PPv, in agreement with the previous studies (7, 22). As the density increases with increasing iron content and therefore the bulk sound velocities (V_Φ) of Pv and PPv are depressed by ~12% and ~10% at 80 to 140 GPa, respectively, compared to those of MgPv and MgPPv.

The computed nine static elastic constants (c_{ij}) and the aggregate bulk (K) and shear moduli (G) of Pv and PPv in $(Fe^{2+}_{0.75}Fe^{3+}_{0.25})(Fe^{3+}_{0.25}Si_{0.75})O_3$ at 60 to 140 GPa are listed in *SI Appendix*, Table S3. We then calculated the compressional (V_P) and shear velocity (V_S) of Pv and PPv as a function of pressure and plotted

Downloaded from https://www.pnas.org by ZHEJIANG UNIVERSITY on April 18, 2024 from IP address 210.32.3.81.

the results in Fig. 3*D*. For the $MgSiO_3$ endmember, previous studies are in general agreement on the jump of V_P and V_S across the Pv-PPv phase transition (13, 32, 37). The calculated curves of V_P and V_S of Pv- and PPv-$(Fe^{2+}_{0.75}Fe^{3+}_{0.25})(Fe^{3+}_{0.25}Si_{0.75})O_3$ as a function of pressure are nearly parallel to those of $MgSiO_3$ (31, 32), with a reduction of ~17% in V_P and ~25% in V_S, respectively. We obtained an increase of 0.7% in V_P and 2.2% in V_S associated with the Pv-PPv phase transition in $(Fe^{2+}_{0.75}Fe^{3+}_{0.25})(Fe^{3+}_{0.25}Si_{0.75})O_3$ at 136 GPa.

Geochemical and Geophysical Implications. The physical and chemical models of the lower mantle are largely dependent on the chemical composition of the silicate phases under *P-T* conditions of the lower mantle. To the best of our knowledge, $(Fe^{2+}_{0.75}Fe^{3+}_{0.25})(Fe^{3+}_{0.25}Si_{0.75})O_3$ Pv and PPv are the densest phases among all the reported silicates stable at *P-T* conditions of the lower mantle, which contains about 25 mol% Fe_2O_3. Under *P-T* conditions of the topmost lower mantle, only up to 16% Fe^{3+} was obtained in (Mg, Fe)SiO_3-Pv (38, 39), indicating that a higher concentration of Fe^{3+} is stabilized in the Pv phase with increasing pressure. Our results further indicate that the disproportionation of ferrous iron into ferric iron plus metallic iron occurs in Al-free compositions under *P-T* conditions of DLM. While all iron in $FeSiO_3$ is located in the Mg-site and remains in a high-spin state (14), 40% iron in $(Fe^{2+}_{0.75}Fe^{3+}_{0.25})(Fe^{3+}_{0.25}Si_{0.75})O_3$ is in the Fe^{3+} state and half Fe^{3+} occupies the Si-site which undergoes a high-spin to low-spin transition above ~55 GPa. The spin-state crossover of ferric iron not only influences the physical properties of the silicate phase but significantly affects the element partitioning between the lower mantle phases (40, 41). The ferric iron content in the silicate phase and the spin-state crossover of Fe^{3+} at the Si-site should be taken into account in order to interpret the seismic observations and construct reliable lower mantle models.

We obtained a smaller increase in V_P than V_S for $(Fe^{2+}_{0.75}Fe^{3+}_{0.25})(Fe^{3+}_{0.25}Si_{0.75})O_3$ associated with the Pv-PPv phase transition, similar to the changes in V_P and V_S for $MgSiO_3$ (31, 32), hence incorporation of $(Fe^{2+}_{0.75}Fe^{3+}_{0.25})(Fe^{3+}_{0.25}Si_{0.75})O_3$ into $MgSiO_3$ has a negligible effect on the jump of seismic velocities across the Pv-to-PPv transition. The iron silicate Pv and PPv can be regarded as solid solutions between $FeSiO_3$ and Fe_2O_3. How the $Fe^{3+}/\sum Fe$ ratio can affect the elastic properties of bridgmanite is a topic of continuing debate. Recent experimental measurements suggested that the V_S of Fe^{3+}-rich Al-bearing bridgmanite as a function of pressure has a steeper slope than that of Fe^{2+}-rich Al-free bridgmanite below 40 GPa (42, 43), in contrast to the finding of our study above 60 GPa that the V_S slope of $(Fe^{2+}_{0.75}Fe^{3+}_{0.25})(Fe^{3+}_{0.25}Si_{0.75})O_3$ as a function of pressure is almost parallel to that of $MgSiO_3$. Based on the previous calculations (13, 44), incorporation of Al_2O_3 also would not explain the steep V_S slope of bridgmanite $(Mg_{0.9}\ Fe_{0.1}\ Si_{0.9}\ Al_{0.1})O_3$ as a function of pressure (42). Furthermore, the first-principles molecular dynamics simulations (45) produce V_S of bdg about 1% smaller than the experimental data at ~2,700 K and lower mantle pressures (46). Effect of chemistry on the elasticity of bdg under *P-T* conditions of the lower mantle will require further clarification.

The ultralow velocity zones (ULVZs) located at the base of the lowermost mantle show great reductions in both V_P and V_S of up to 15% and 30%, respectively, as well as a notable increase in density and Poisson's ratio (ν) (47). Iron enrichment in PPv has been proposed as a potential origin for ULVZs on the basis of acoustic velocities of iron-rich PPv (48). We obtained a ratio of P-wave and S-wave velocity reduction of ~1.5 for $(Fe^{2+}_{0.75}Fe^{3+}_{0.25})(Fe^{3+}_{0.25}Si_{0.75})O_3$-PPv at the CMB pressure, while most of the reported ULVZs with about 30% reduction in V_S have the ratio close to 3:1 (49). Therefore, our results suggest that the elastic properties of $(Fe^{2+}_{0.75}Fe^{3+}_{0.25})(Fe^{3+}_{0.25}Si_{0.75})O_3$-PPv alone may not explain the seismic characteristics of the ULVZs. Dehydration of dense hydrous phases under high *P-T* conditions at the CMB could induce partial melting (50) and contribute to the distinct physicochemical properties of the ULVZs. Seismic observations support a vertical connection between broad plumes and the large-scale low shear-velocity anomalies at the base of the lower mantle, some of which coincide with the location of ULVZs (51). Our results of the stability and physical properties of iron silicates Pv and PPv would place constraints on the extent of iron-enrichment of these low shear-velocity anomalies in the DLM.

Data, Materials, and Software Availability. All study data are included in the article and/or *SI Appendix*.

ACKNOWLEDGMENTS. This work was supported by the National Natural Science Foundation of China (grant nos. 42150103 and 41925017). H.-k.M. acknowledges financial support from Shanghai Key Laboratory Novel Extreme Condition Materials, China (no. 22dz2260800), Shanghai Science and Technology Committee, China (no. 22JC1410300) and National Science Foundation of China (grant no. U2230401). The XRD experiments were performed at BL15U1 of the Shanghai Synchrotron Radiation Facility (SSRF). The computations were conducted in the Supercomputing Center of the University of Science and Technology of China.

Author affiliations: [a]Center for High Pressure Science and Technology Advanced Research, Shanghai 201203, China; [b]Laboratory of Seismology and Physics of Earth's Interior, School of Earth and Space Sciences, University of Science and Technology of China, Hefei, Anhui 230026, China; [c]Chinese Academy of Sciences Center for Excellence in Comparative Planetology, University of Science and Technology of China, Hefei, Anhui 233500, China; [d]National Geophysical Observatory at Mengcheng, University of Science and Technology of China, Hefei, Anhui 233500, China; and [e]Shanghai Key Laboratory MFree, Institute for Shanghai Advanced Research in Physical Sciences, Shanghai 201203, China

1. A. Ricolleau *et al.*, Density profile of pyrolite under the lower mantle conditions. *Geophys. Res. Lett.* **36**, L06302 (2009).
2. R. D. van der Hilst, H. Kárason, Compositional heterogeneity in the bottom 1000 kilometers of Earth's mantle: Toward a hybrid convection model. *Science* **283**, 1885–1888 (1999).
3. M. Ishii, J. Tromp, Normal-mode and free-air gravity constraints on lateral variations in velocity and density of Earth's mantle. *Science* **285**, 1231–1236 (1999).
4. J. Trampert, F. Deschamps, J. Resovsky, D. Yuen, Probabilistic tomography maps chemical heterogeneities throughout the lower mantle. *Science* **306**, 853–856 (2004).
5. Y. Tange, E. Takahashi, Y. Nishihara, K. I. Funakoshi, N. Sata, Phase relations in the system MgO-FeO-SiO_2 to 50 GPa and 2000°C: An application of experimental techniques using multianvil apparatus with sintered diamond anvils. *J. Geophys. Res. Solid Earth* **114**, B02214 (2009).
6. T. Arimoto *et al.*, Phase relations of $MgSiO_3$-$FeSiO_3$ system up to 64 GPa and 2300 K using multianvil apparatus with sintered diamond anvils. *Phys. Earth Planet. Inter.* **295**, 106297 (2019).
7. S. M. Dorfman, Y. Meng, V. B. Prakapenka, T. S. Duffy, Effects of Fe-enrichment on the equation of state and stability of (Mg, Fe)Si_03 perovskite. *Earth Planet Sci. Lett.* **361**, 249–257 (2013).
8. W. L. Mao *et al.*, Iron-rich silicates in the Earth's D″ layer. *Proc. Natl. Acad. Sci. U.S.A.* **102**, 9751–9753 (2005).
9. A. E. Ringwood, The constitution of the mantle-II Further data on the olivine-spinel transition. *Geochim. Cosmochim. Acta* **15**, 18–29 (1958).
10. H. K. Mao, P. M. Bell, High pressure decomposition of spinel (Fe_2SiO_4). *Year Book Carnegie Inst. Washington* **70**, 176–178 (1971).
11. W. A. Bassett, L.-C. Ming, Disproportionation of Fe_2SiO_4 to $2FeO+SiO_2$ at pressures up to 250 kbar and temperatures up to 3000 K. *Phys. Earth Planet. Inter.* **6**, 154–160 (1972).
12. K. Fujino *et al.*, Stability of the perovskite structure and possibility of the transition to the post-perovskite structure in $CaSiO_3$, $FeSiO_3$, $MnSiO_3$ and $CoSiO_3$. *Phys. Earth Planet. Inter.* **177**, 147–151 (2009).
13. R. Caracas, R. E. Cohen, Effect of chemistry on the stability and elasticity of the perovskite and post-perovskite phases in the $MgSiO_3$-$FeSiO_3$- Al_2O_3 system and implications for the lowermost mantle. *Geophys. Res. Lett.* **32**, L16310 (2005).
14. S. Stackhouse, J. P. Brodholt, G. D. Price, Elastic anisotropy of $FeSiO_3$ end-members of the perovskite and post-perovskite phases. *Geophys. Res. Lett.* **33**, L01304 (2006).
15. R. E. Cohen, Y. Lin, Prediction of a potential high-pressure structure of $FeSiO_3$. *Phys. Rev. B* **90**, 140102 (2014).
16. L. Ismailova *et al.*, Stability of Fe, Al-bearing bridgmanite in the lower mantle and synthesis of pure Fe-bridgmanite. *Sci. Adv.* **2**, e1600427 (2016).

Downloaded from https://www.pnas.org by ZHEJIANG UNIVERSITY on April 18, 2024 from IP address 210.32.3.81.

17. H. St. C. O'Neill, The origin of the moon and the early history of the Earth–A chemical model. Part 2: The earth. *Geochim. Cosmochim. Acta* **55**, 1159–1172 (1991).
18. Y. Fei *et al.*, Toward an internally consistent pressure scale. *Proc. Natl. Acad. Sci. U.S.A.* **104**, 9182–9186 (2007).
19. Y. Akahama, H. Kawamura, Pressure calibration of diamond anvil Raman gauge to 310 GPa. *J. Appl. Phys.* **100**, 043516 (2006).
20. H. Yuan *et al.*, Stability of Fe-bearing hydrous phases and element partitioning in the system MgO–Al_2O_3–Fe_2O_3–SiO_2–H_2O in Earth's lowermost mantle. *Earth Planet Sci. Lett.* **524**, 115714 (2019).
21. W. L. Mao *et al.*, Ferromagnesian post-perovskite silicates in the D″ layer of the Earth. *Proc. Natl. Acad. Sci. U.S.A.* **101**, 15867–15869 (2004).
22. S. M. Dorfman, T. S. Duffy, Effect of Fe-enrichment on seismic properties of perovskite and post-perovskite in the deep lower mantle. *Geophys. J. Int.* **197**, 910–919 (2014).
23. K. Catalli *et al.*, Spin state of ferric iron in $MgSiO_3$ perovskite and its effect on elastic properties. *Earth Planet Sci. Lett.* **289**, 68–75 (2010).
24. S. Lundin *et al.*, Effect of Fe on the equation of state of mantle silicate perovskite over 1 Mbar. *Phys. Earth Planet. Inter.* **168**, 97–102 (2008).
25. J. Liu *et al.*, Valence and spin states of iron are invisible in Earth's lower mantle. *Nat. Commun.* **9**, 1284 (2018).
26. N. Guignot, D. Andrault, G. Morard, N. Bolfan-Casanova, M. Mezouar, Thermoelastic properties of post-perovskite phase $MgSiO_3$ determined experimentally at core-mantle boundary P-T conditions. *Earth Planet Sci. Lett.* **256**, 162–168 (2007).
27. S. R. Shieh *et al.*, Equation of state of the postperovskite phase synthesized from a natural (Mg,Fe) SiO_3 orthopyroxene. *Proc. Natl. Acad. Sci. U.S.A.* **103**, 3039–3043 (2006).
28. L. Zhang, Y. Meng, W. L. Mao, Effect of pressure and composition on lattice parameters and unit-cell volume of (Fe, Mg)Si_O3 post-perovskite. *Earth Planet Sci. Lett.* **317–318**, 120–125 (2012).
29. S. Tateno, K. Hirose, N. Sata, Y. Ohishi, Determination of post-perovskite phase transition boundary up to 4400 K and implications for thermal structure in D″ layer. *Earth Planet Sci. Lett.* **277**, 130–136 (2009).
30. J. M. Brown, T. J. Shankland, Thermodynamic parameters in the Earth as determined from seismic profiies. *Geophys. J. R. astr. Soc.* **66**, 579–596 (1981).
31. R. M. Wentzcovitch, B. B. Karki, M. Cococcioni, S. de Gironcoli, Thermoelastic properties of $MgSiO_3$-perovskite: Insights on the nature of the Earth's lower mantle. *Phys. Rev. Lett.* **92**, 018501 (2004).
32. T. Tsuchiya, J. Tsuchiya, K. Umemoto, R. M. Wentzcovitch, Elasticity of post-perovskite $MgSiO_3$. *Geophys. Res. Lett.* **31**, L14603 (2004).
33. S. Ono, Y. Ohishi, In situ X-ray observation of phase transformation in Fe_2O_3 at high pressures and high temperatures. *J. Phys. Chem. Solids.* **66**, 1714–1720 (2005).
34. E. Bykova *et al.*, Structural complexity of simple Fe_2O_3 at high pressures and temperatures. *Nat. Commun.* **7**, 10661 (2016).
35. G. Shukla, R. M. Wentzcovitch, Spin crossover in (Mg, F^{e3}+)(Si, ^{Fe}3+)O3 bridgmanite: Effects of disorder, iron concentration, and temperature. *Phys. Earth Planet. Inter.* **260**, 53–61 (2016).
36. W. Wang *et al.*, Formation of large low shear velocity provinces through the decomposition of oxidized mantle. *Nat. Commun.* **12**, 1911 (2021).
37. S. Stackhouse, J. P. Brodholt, J. Wookey, J. M. Kendall, G. D. Price, The effect of temperature on the seismic anisotropy of the perovskite and post-perovskite polymorphs of $MgSiO_3$. *Earth Planet Sci. Lett.* **230**, 1–10 (2005).
38. C. McCammon, Perovskite as a possible sink for ferric iron in the lower mantle. *Nature* **387**, 694–696 (1997).
39. Y. Fei, D. Virgo, B. O. Mysen, Y. Wang, H. K. Mao, Temperature-dependent electron delocalization in (Mg, Fe)Si_O3 perovskite. *Am. Mineral.* **79**, 826–837 (1994).
40. J. Badro *et al.*, Iron partitioning in earth's mantle: Toward a deep lower mantle discontinuity. *Science* **300**, 789–791 (2003).
41. H. Piet *et al.*, Spin and valence dependence of iron partitioning in Earth's deep mantle. *Proc. Natl. Acad. Sci. U.S.A.* **113**, 11127–11130 (2016).
42. A. Kurnosov, H. Marquardt, D. J. Frost, T. Boffa Ballaran, L. Ziberna, Evidence for a Fe^{3+}-rich pyrolitic lower mantle from (Al, Fe)-bearing bridgmanite elasticity data. *Nature* **543**, 543–546 (2017).
43. I. Mashino, M. Murakami, N. Miyajima, S. Petitgirard, Experimental evidence for silica-enriched Earth's lower mantle with ferrous iron dominant bridgmanite. *Proc. Natl. Acad. Sci. U.S.A.* **117**, 27899–27905 (2020).
44. S. Stackhouse, J. P. Brodholt, G. D. Price, High temperature elastic anisotropy of the perovskite and post-perovskite polymorphs of Al_2O_3. *Geophys. Res. Lett.* **32**, L13305 (2005).
45. Z. Zhang, L. Stixrude, J. Brodholt, Elastic properties of $MgSiO_3$-perovskite under lower mantle conditions and the composition of the deep Earth. *Earth Planet Sci. Lett.* **379**, 1–12 (2013).
46. M. Murakami, Y. Ohishi, N. Hirao, K. Hirose, A perovskitic lower mantle inferred from high-pressure, high-temperature sound velocity data. *Nature* **485**, 90–94 (2012).
47. M. S. Thorne, E. J. Garnero, Inferences on ultralow-velocity zone structure from a global analysis of SPdKS waves. *J. Geophys. Res. Solid Earth* **109**, B08301 (2004).
48. W. L. Mao *et al.*, Iron-rich post-perovskite and the origin of ultralow-velocity zones. *Science* **312**, 564–565 (2006).
49. S. Yu, E. J. Garnero, Ultralow velocity zone locations: A global assessment. *Geochem. Geophys. Geosys.* **19**, 396–414 (2018).
50. Y. Lin, H. K. Mao, Dense hydrous silica carrying water to the deep Earth and promotion of oxygen fugacity heterogeneity. *Matter Radiat. Extrem.* **7**, 068101 (2022).
51. S. W. French, B. Romanowicz, Broad plumes rooted at the base of the Earth's mantle beneath major hotspots. *Nature* **525**, 95–99 (2015).

Downloaded from https://www.pnas.org by ZHEJIANG UNIVERSITY on April 18, 2024 from IP address 210.32.3.81.